Full Text View

Volume 30, Issue 3 (March 2000)

Journal of Physical Oceanography
Article: pp. 572–589 | Abstract | PDF (665K)

A Study of the Balance of Horizontal Momentum in a Vertical Shearing Current

Álvaro Viúdez and Robert L. Haney

Departament de Física, Universitat de les Illes Balears, Palma de Mallorca, Spain

John T. Allen

Southampton Oceanography Centre, Southampton, United Kingdom

(Manuscript received November 12, 1998, in final form April 12, 1999)

DOI: 10.1175/1520-0485(2000)030<0572:ASOTBO>2.0.CO;2

ABSTRACT

Horizontal current and density data fields are analyzed in order to validate, from an experimental point of view, the contribution of the advective and Coriolis accelerations and the hydrostatic pressure gradient term to the balance of horizontal momentum. The relative importance of the vertical advection of horizontal velocity in this balance is estimated by solving the quasigeostrophic (QG) omega equation. The analysis of the balance of horizontal momentum is carried out using data from three consecutive high-resolution samplings of the Atlantic jet (AJ) and western Alboran gyre (WAG) on the eastern side of the Strait of Gibraltar.

The horizontal velocity reached maximum values of 1.30 m s^{-1} in the AJ at the surface. The ageostrophic velocity field reaches maximum absolute values of 30 cm s^{-1} at the surface, thus confirming the supergeostrophic nature of the AJ. At the surface the pressure gradient term reaches absolute values of 8–10 ($\times 10^{-5}$ m s^{-2}), the Coriolis acceleration 10–12 ($\times 10^{-5}$ m s^{-2}), and the advective horizontal acceleration 3×10^{-5} m s^{-2}. The vertical advection of horizontal velocity by the QG vertical velocity at 100 m is one order of magnitude smaller [$O(10^{-6}$ m $s^{-2})$].

The *geostrophic imbalance* (difference between the pressure gradient term and the Coriolis acceleration) reaches 5×10^{-5} m s^{-2} at the surface. The *gradient imbalance* (defined as the difference between the pressure gradient term and the Coriolis plus advective accelerations) is smaller than the geostrophic

imbalance (being of order 2.5×10^{-5} m s^{-2}) making gradient balance the best estimate of the balance of horizontal momentum given the characteristics (synopticity and experimental errors) of the analyzed dataset.

The gradient imbalance is not uniform in the horizontal but rather is larger in the AJ than in the WAG. From this result it is inferred that the AJ current experiences larger variations (larger local acceleration) than the WAG current.

1. Introduction

The balance of horizontal momentum is the fundamental dynamical balance that holds in hydrostatic flows. It is therefore of importance to investigate the dynamics of the flow in a given portion of the ocean by means of the relative contribution of the different terms in this balance. In a rotating frame, the momentum balance relates the local, advective (horizontal and vertical advections), and Coriolis accelerations to the total pressure gradient term. Among these terms the vertical advection of horizontal velocity ($w\partial\mathbf{u}/\partial z$) and the total pressure gradient term are the most difficult to measure in large-scale oceanic flows. Furthermore, conventional oceanographic cruises usually have to choose between high temporal resolution capable of measuring the local acceleration ($\partial\mathbf{u}/\partial t$) and high spatial resolution capable of measuring the advective acceleration ($\mathbf{u} \cdot \nabla\mathbf{u}$). As a consequence, an accurate determination of the total acceleration field is rarely achieved.

However in those situations where the spatial velocity and density fields are known it is possible to validate, from an experimental point of view, the contribution of the advective and Coriolis accelerations and the contribution of the pressure gradient term (using the hydrostatic approximation) to this horizontal momentum balance. The objective of this study is to develop this task.

The theoretical basis is briefly described in section 2. In section 3 the momentum balance analysis is carried out for three consecutive high-resolution samplings of the Atlantic jet (AJ) and western Alboran gyre (WAG) at the eastern side of the Strait of Gibraltar (Western Mediterranean). The results are summarized in section 4. It is found that the *gradient imbalance* (defined as the difference between the pressure gradient term and the Coriolis plus advective accelerations) is smaller than the geostrophic imbalance and therefore gradient balance is considered to be the best estimate of the balance of horizontal momentum given the characteristics (synopticity and experimental errors) of the analyzed dataset.

2. The balance of horizontal momentum

In this section we first review (for the sake of defining the different quantities further referenced) the relations between the velocity and density data obtained in conventional oceanographic cruises. The hydrostatic equation may be written

$$P_{,z}(\mathbf{x}, z) = -g\rho(\mathbf{x}, z). \quad (1)$$

Here $h_{,x}$ indicates the partial derivative of the function h with respect to the variable x, ρ is the density field, $\alpha \equiv \rho^{-1}$ is the specific volume, and g is the acceleration due to gravity. Vertical integration of (1) yields

$$P(\mathbf{x}, z) = P(\mathbf{x}, z_1) - g \int_{z_1}^{z} \rho(\mathbf{x}, z')\, dz'. \quad (2)$$

Let ∇ denote the gradient in the xy plane in the $(\mathbf{x}, z)$ space. The gradient of (2) is

$$\nabla P(\mathbf{x}, z) = \nabla P(\mathbf{x}, z_1) - g \int_{z_1}^{z} \nabla\rho(\mathbf{x}, z')\, dz'. \quad (3)$$

The second term on the rhs of (3) is here called the *pressure anomaly* gradient.

Though geostrophic velocities are merely a name for the rotated and scaled pressure gradient field, and therefore their use is not strictly needed in the dynamics presented here, we will introduce them next, and compute them in the next section, because of the extensive practice of thinking in terms of geostrophic velocity rather than in terms of rotated pressure gradient. The pressure anomaly is used to define the streamfunction of the *geostrophic velocity* $\mathbf{u}^g$ at level z

$$\mathbf{u}^g(\mathbf{x}, z) \equiv \alpha\, f^{-1}\mathbf{k} \times \nabla P(\mathbf{x}, z), \quad (4)$$

where $\alpha_0 \equiv \rho^{-1}{}_0$, ρ_0 is a constant reference density, and f is the Coriolis parameter (here assumed to be constant). For hydrostatic flow, using (3),

$$\mathbf{u}^g(\mathbf{x}, z) = \mathbf{u}^g(\mathbf{x}, z_1) - \mathbf{k} \times \nabla[\Psi(\mathbf{x}, z_1, z)/f], \quad (5)$$

where

$$\Psi(\mathbf{x}, z_1, z) \equiv g\alpha_0 \int_{z_1}^{z} \rho(\mathbf{x}, z')\, dz'. \quad (6)$$

The quantity Ψ/f is the streamfunction of $\mathbf{u}^g(\mathbf{x}, z) - \mathbf{u}^g(\mathbf{x}, z_1)$. Thus, for hydrostatic flows, the geostrophic shear is

$$\mathbf{u}^g{}_{,z}(\mathbf{x}, z) \equiv -g\alpha_0 f^{-1}\mathbf{k} \times \nabla\rho(\mathbf{x}, z). \quad (7)$$

We use the horizontal momentum equation for three-dimensional motion under the f-plane and Boussinesq approximations

$$\begin{aligned} &\mathbf{u}_{,t} + \mathbf{u} \cdot \nabla\mathbf{u} + w\mathbf{u}_{,z} + f\mathbf{k} \times \mathbf{u} \\ &\quad = -\alpha_0 \nabla P + \mathbf{F} \\ &\quad = -\nabla\Psi(\mathbf{x}, z_1, z) - \alpha_0 \nabla P(\mathbf{x}, z_1) + \mathbf{F}, \end{aligned} \quad (8)$$

where $\mathbf{u}_{,t}$ is the local acceleration, $\mathbf{u} \cdot \nabla\mathbf{u}$ is the horizontal advective acceleration, and $w\mathbf{u}_{,z}$ is the vertical advection of horizontal velocity; $\mathbf{F}(\mathbf{x}, z)$ represents a generic term including friction or other forcing. The pressure P has been partioned using (2) and (6). The term $-\alpha_0 \nabla P(\mathbf{x}, z_1)$ is sometimes called the barotropic pressure force. When the $\mathbf{u}$ and ρ fields (but not $\mathbf{u}_{,t}$) are known, and for a fixed reference level z_1, we can compute at every point $(\mathbf{x}, z)$ the terms

$$\begin{aligned} \mathbf{I}_0(\mathbf{x}, z_1, z) &\equiv -\nabla\Psi(\mathbf{x}, z_1, z) - f\mathbf{k} \times \mathbf{u}, \\ \mathbf{I}_1(\mathbf{x}, z_1, z) &\equiv -\nabla\Psi(\mathbf{x}, z_1, z) - (\mathbf{u} \cdot \nabla\mathbf{u} + f\mathbf{k} \times \mathbf{u}). \end{aligned} \quad (9)$$

The fields $\mathbf{I}_0$ and $\mathbf{I}_1$ are referred to here as the *geostrophic imbalance* and the *gradient imbalance*, respectively. We assume that a certain deep level z_0 exists where the flow is steady [$\mathbf{u}_{,t}(\mathbf{x}, z_0) = \mathbf{0}$] and select it as the reference level ($z_1 = z_0$). At that level (and neglecting $\mathbf{F}$) we obtain $\alpha_0 \nabla P(\mathbf{x}, z_0) = -(\mathbf{u} \cdot \nabla\mathbf{u} + w\mathbf{u}_{,z} + f\mathbf{k} \times \mathbf{u})|_{z=z_0}$. [In this study the vertical velocity is approximated by its quasigeostrophic (QG) part and computed from the QG omega equation. For the sake of generality, the vertical advection term $w\mathbf{u}_{,z}$ is retained in this expression, though in practice it can be neglected.] We will choose z_0 as a deep enough layer (253-m depth) where the horizontal velocity field is negligible (in fact, below the accuracy of the current measurements) compared with that at the upper levels (say, $z = -100$ m). This is simply a special case of using the method of level of known and zero motion, being consistent with previous studies in the region that have used a level of no motion near 200 m (Parrilla and Kinder 1987; Perkins et al. 1990).

In the next section we follow the above scheme to study the Atlantic jet and western Alboran gyre circulation present in the western Alboran basin. Specifically we will examine the geostrophic and gradient imbalances given by (9). Since both of these imbalances may reflect the effect of wind and tidal forcing, we have reason to expect that they will not be small in the near-surface layers where such forcing is known to be significant.

3. The balance of horizontal momentum in the western Alboran Sea

There is an abundant bibliography on both the description and numerical and laboratory simulation of the AJ–WAG dynamics. The reader is referred to Parrilla and Kinder (1987) for a general description; Bucca and Kinder (1984) for meteorological effects; Gascard and Richez (1985) and Parrilla et al. (1986) for water masses; La Violette (1986) for short-term variability, Heburn and La Violette (1990) and Viúdez et al. (1998) for the surface circulation and gyre's variability,

Perkins et al. (1990) for the Atlantic inflow, Viúdez et al. (1996a, 1996b) for the gyre's structure and ageostrophic motion, Viúdez and Haney (1997) for a vorticity analysis, Vázquez-Cuervo et al. (1996) for altimeter data analysis, Whitehead and Miller (1979), Whitehead (1985), Gleizon et al. (1996) for laboratory simulations, and Speich et al. (1996) for numerical simulations. None of the above studies has specifically addressed the momentum budget as done here.

a. The dataset

We shall use velocity and density data from three consecutive surveys of the AJ and northern part of the WAG system carried out in October 1996 as part of the OMEGA (Observation and Modelling of Eddy Scale Geostrophic and Ageostrophic Circulation) project, and current meter data from the "Donde Va?" experiment (June–October 1982). The three surveys were made using the towed undulating CTD instrument, SeaSoar, an RDI 150-kHz vessel-mounted acoustic Doppler current profiler (VM-ADCP); 3D GPS ship's heading information and differential GPS navigation. Each survey had a duration of ~ 2.5 days and consisted of 9–11 parallel north–south legs ~ 80 km long and ~ 10 km apart [see Allen et al. (1997) for details of SeaSoar, navigation, and VM-ADCP data processing]. After routine processing and calibration SeaSoar data were equivalent to CTD stations at an alongtrack spacing of ~ 4 km and to a depth of 350 m (Fig. 1). The calibration of VM-ADCP data was less routine. The VM-ADCP is capable of determining the three-dimensional motion of fluid particles in the upper 200–300 m of the water column, relative to the axes of the instrument, to an instrumental accuracy of 1 cm s^{-1}. However, when deriving the absolute water velocities, significantly larger errors (typically 10 cm s^{-1}) generally arise from inaccuracy in ship velocity measurement and misalignment between the axes of the ADCP and the ship. To reduce this error, real time corrected differential GPS navigation was purchased through RACAL SKYFIX for the duration of the cruise to reduce errors in the determination of the ship's velocity by one order of magnitude (<1 cm s^{-1} for 10-min averages). The misalignment of the ADCP was calibrated using the method of Pollard and Read (1989). An Ashtech 3D GPS system was used to correct ship's heading data: the 3D GPS system uses the phase differences between the signal received at four antennas to determine the orientation of the ship (Allen et al. 1997). As a result the processed VM-ADCP data consisted of 10-min averaged current velocity profiles to a depth of ~ 300 m. Each profile had a vertical data resolution of 4 m and, away from extreme depths (e.g., over the range 8–250 m), an estimated accuracy of 1 cm s^{-1}.

Temperature, salinity, and ADCP components ($u_{(x)}$, $u_{(y)}$) at every vertical level were again interpolated from the equivalent CTD stations onto a regular grid using a method of successive corrections (Brathset 1986; Franke 1988) in the same way as used in Viúdez et al. (1996a). The grid was 41 × 41 × 31 nodes, resulting in a grid spacing of $\delta x \approx 3$ km, $\delta y \approx 2.3$ km, and $\delta z = 8$ m. Keeping in mind that every survey was completed in about 2.5 days we shall assume, before drawing conclusions about the temporal variability of the measured fields, that every survey is synoptic. We are furnished therefore with a certain *model* (the interpolated fields) of the synoptic state of the ocean from which we begin our analysis.

b. The density field

The density field as represented by conventional potential density anomaly ($\sigma_\theta \equiv \rho_\theta - 10^3$ kg m^{-3}, where ρ_θ is potential density) at 100 m for the three consecutive surveys is shown in Fig. 1.

During the first survey (No. 1) the AJ–WAG system occupied most of the northern part of the western Alboran basin. The WAG at this depth, approximately separated from the AJ by the density interval $\sigma_\theta \subset (27.0,\ 27.2)$, is characterized by relatively low density values $\sigma_\theta \subset (26.1,\ 27.0)$. The water of the AJ [$\sigma_\theta \subset (27.2,\ 28.4)$ and therefore denser than the water of the WAG] surrounds the northern part of the WAG, practically reaching the Iberian coast. Some temporal variability can be seen from the change in the σ_θ distribution from the first to the second survey (No. 2). The WAG has become smaller, the AJ front in the western part of the domain has compressed and shifted southward, while in the eastern part of the domain it has spread and shifted northward. The σ_θ distribution during the third survey (No. 3) shows Atlantic waters entering into the western Alboran basin as a nearly straight jet distorting the previously almost circular shape of the WAG. This time variability of the circulation in the Alboran Sea took place before the eastward migration of the WAG that was observed from satellite thermal imagery to occur between 20 October and the end of November 1996 (Viúdez et al. 1998). The horizontal density gradients in the AJ–WAG system during survey 1 (Fig. 2) reached 250 m, which is somewhat deeper than normal for this upper-layer system (200–230 m).

c. The vertical shear and the reference level

As mentioned in the previous section, the reference level where $\mathbf{u}_{,t} \sim \mathbf{0}$ is assumed to be the level where the ADCP current signal was below the determined accuracy of the current measurements [about 8 cm s^{-1} (see appendix A)]. This level is also where the bottom boundary condition for the QG vertical velocity (w^{QG}) is assumed to be zero and coincides

with the layer where the vertical shear is minimal. Let the horizontally averaged magnitude of any field $A(\mathbf{x}, z)$ be defined as

$$\langle A(\mathbf{x}, z)\rangle \equiv N^{-1} \sum_{i=1}^{N} A(\mathbf{x}_i, z), \qquad (10)$$

with N the number of grid points in the horizontal. The vertical dependence of the horizontally averaged magnitude of the interpolated ADCP data $\langle|\mathbf{u}|\rangle$ is shown for the three surveys in Fig. 3a. It reaches maximum values of about 80 cm s^{-1} at the surface, while it decreases to 8 cm s^{-1} below 200 m. The magnitude of the vertical shear (Fig. 4) shows that $|\mathbf{u}_{,z}|$ has maximum values of 10×10^{-3} s^{-1} in the upper 180 m associated with the AJ. Below 180 m, there are layers where $|\mathbf{u}_{,z}| < 10^{-3}$ s^{-1}. The horizontally averaged magnitude of the vertical shear $\langle|\mathbf{u}_{,z}|\rangle$ (Fig. 3b) reaches maximum values of 6×10^{-3} s^{-1} between 50 and 150 m, while it decreases to 1×10^{-3} s^{-1} below 200 m. Horizontal density gradients, and therefore the shear of the geostrophic current, are higher in the first 200 m. It is therefore concluded that any level below 200 m can be selected as the reference level. In this study we choose the reference level $z_1 = z_0 = -253$ m (the data level closest to 250 m). The horizontal spatial variability of the $\mathbf{u}_{,z}$ field at 253 m (Fig. 5) shows that in most of the domain $|\mathbf{u}_{,z}|$ is smaller than 2×10^{-3} s^{-1}. By selecting $z_1 = -253$ m our reference level is still similar to that traditionally used to compute geostrophic velocities in the Alboran Sea, so that the baroclinic pressure term $\nabla\Psi(\mathbf{x}, z_1, z)$ can be used to compare actual with previously computed geostrophic velocities and geostrophic transports.

d. The relative geostrophic transport

In order to have an idea of the volume transport involved in this system, it is useful to examine the *relative geostrophic transport function* $Q_{z_1}(\mathbf{x}, z)$. The relative geostrophic transport between two vertical levels z_1 and z, across a horizontal path $\mathbf{x} = \mathcal{L}(s)$, is defined by

$$\begin{aligned}
&\int_{z_1}^{z}\int_{\mathcal{L}} [\mathbf{u}^g(\mathbf{x}, z') - \mathbf{u}^g(\mathbf{x}, z_1)] \cdot (d\mathbf{x} \times \mathbf{k})\, dz' \\
&\quad = \int_{z_1}^{z}\int_{\mathcal{L}} f^{-1}\nabla\Psi(\mathbf{x}, z_1, z') \cdot d\mathbf{x}\, dz' \\
&\quad = \int_{\mathcal{L}} dQ_{z_1}(\mathbf{x}, z), \qquad (11)
\end{aligned}$$

where

$$\begin{aligned}
Q_{z_1}(\mathbf{x}, z) &\equiv f^{-1}\int_{z_1}^{z} \Psi(\mathbf{x}, z_1, z')\, dz' \\
&= g\alpha_0 f^{-1}\int_{z_1}^{z} (z - z')\rho(\mathbf{x}, z')\, dz'. \qquad (12)
\end{aligned}$$

The last result in (12) is obtained after using (6) and integrating by parts (see, e.g., JPOTS 1991 for the geostrophic transport function in pressure coordinates). Thus, from (11), the difference between two values of Q_{z_1} at different locations $\mathbf{x}_1$ and $\mathbf{x}_2$, that is, $Q_{z_1}(\mathbf{x}_1, z) - Q_{z_1}(\mathbf{x}_2, z)$, gives the net volume transport by the relative geostrophic velocity through the area limited by the two vertical levels z_1 and z and any horizontal path $\mathcal{L}$ connecting $\mathbf{x}_2$ and $\mathbf{x}_1$. The WAG and AJ are distinguished because the WAG has closed streamlines (usually computed geostrophically) while the AJ has open

streamlines. Since the WAG was not completely sampled during the three surveys, we are forced to identify the boundary streamline (the edge between WAG and AJ) as that streamline showing a large confluence in the western limit of the sampled domain (Fig. 6). This occurs for streamlines labeled 0.2, 0, and 0.2, for the three cruises, respectively. The average relative geostrophic transport of the WAG for the three surveys is approximately 2.6×10^6 m^3 s^{-1}, while that associated with the AJ is about 1.8×10^6 m^3 s^{-1}. These values are relatively large compared to other transport estimates associated to different AJ–WAG states [1.6 for the WAG and 1 ($\times 10^6$ m^3 s^{-1}) for the AJ in Viúdez et al. (1996a)]. Also, the *dynamic height* at the core of the WAG relative to pressure $p_1 \approx 253$ db was about 30 dyn cm, comparable to the largest values observed in the WAG (Lanoix 1974; Cano 1978, Fig. 10).

e. The total and the relative geostrophic velocity

The geostrophic velocity field at $z = -13$ m, relative to $z_1 = -253$ m, is shown in Fig. 7. It has maximum values of 110 cm s^{-1} for the three surveys. In survey 1 there is a relative maximum on both sides of the ridge, while in surveys 2 and 3 the maximum values of $\nabla\Psi$ are located where the AJ pinches in the WAG. Visual comparison of the $\mathbf{u}^g$ field with the ADCP velocity field $\mathbf{u}$ (Fig. 8) shows that, though $\mathbf{u}^g$ provides a broadly similar pattern to $\mathbf{u}$ in the sense that curvature and maxima distributions are similar, clear differences are also observed. Maximum values of $u \equiv |\mathbf{u}|$ at 13 m in the AJ exceed 120, 140, and 130 cm s^{-1} [60, 70, and 60 cm s^{-1}, at 100 m, not shown] for the three surveys, respectively. In particular, the speed u is almost everywhere larger than the geostrophic speed $u^g \equiv |\mathbf{u}^g|$. Introducing the reference frame ($\mathbf{s}$, $\mathbf{n}$) where $\mathbf{s} \equiv \mathbf{u}/u$ (for $u \neq 0$) is the unit tangent vector and $\mathbf{n} \equiv \mathbf{k} \times \mathbf{s}$ is the unit normal vector, the velocity field is simply expressed as $\mathbf{u} \equiv u\mathbf{s}$, and the geostrophic velocity $\mathbf{u}^g = u^g_{(s)}\mathbf{s} + u^g_{(n)}\mathbf{n}$. We define that the flow $\mathbf{u}$ is *supergeostrophic* (*subgeostrophic*) if $u > u^g_{(s)}$, ($u < u^g_{(s)}$). The AJ was therefore primarily supergeostrophic during the first two surveys. We emphasize that this supergeostrophic characteristic of the current is valid for both relative and absolute geostrophic velocities because the horizontal pressure gradient is much smaller at the reference level (see below) than at 100 m.

The ageostrophic velocity $\mathbf{u}^a \equiv \mathbf{u} - \mathbf{u}^g$ at 100 m for the three surveys (Fig. 9) shows that the AJ was supergeostrophic for surveys 1 and 2 and that the WAG was supergeostrophic during the three surveys. In a large part of the domain the ageostrophic velocity ranges between 10 and 20 cm s^{-1}, reaching in some places 30 cm s^{-1}. That the magnitude of this ageostrophic velocity exceeds the errors in the interpolated ADCP data (up to 8 cm s^{-1} as discussed in the appendix) validates the capacity of the ADCP data to measure the large ageostrophic motion in this case and allows us to extend the analysis of the momentum balance beyond the geostrophic equilibrium.

f. The balance of horizontal momentum

To clarify the cause of the geostrophic imbalance, inferred from the difference between $\mathbf{u}(\mathbf{x}, z)$ and $-\mathbf{k} \times \nabla\Psi(\mathbf{x}, z_1, z)/f$, we now analyze the different terms in the momentum equation (8). The analysis is carried out for the three Alboran surveys.

1) THE PRESSURE ANOMALY GRADIENT AND THE CORIOLIS ACCELERATION

The pressure anomaly gradient $-\nabla\Psi(\mathbf{x}, z_1, z)$ at $z = -13$ m relative to the reference level z_1 (Fig. 10), having maxima between 8 and 10 ($\times 10^{-5}$ m s^{-2}) for the three samplings, clearly has a smaller magnitude than the Coriolis acceleration (Fig. 11), which has several relative maxima of 10–12 ($\times 10^{-5}$ m s^{-2}). Also the relative maxima of the pressure anomaly force for the three samplings appear to be somewhat north of the Coriolis acceleration maxima. Thus $\nabla\Psi$ maxima are mainly located in the AJ, while $f\mathbf{k} \times \mathbf{u}$ maxima are located more along the AJ–WAG boundary. Note also that in surveys 2 and 3, the $f\mathbf{k} \times \mathbf{u}$ maxima are shifted downstream of $\nabla\Psi$ maxima.

2) THE ADVECTIVE ACCELERATION

The magnitude of the advective acceleration $\mathbf{u} \cdot \nabla\mathbf{u}$ (Fig. 12) has maximum values of 3, 5, and 3 ($\times 10^{-5}$ m s^{-2}) at 13 m (1.5×10^{-5} m s^{-2} at 100 m, not shown) for the three surveys, which are smaller than, but still a significant fraction of, the Coriolis acceleration. In general, the advective acceleration has a large component opposite to the Coriolis acceleration. This component of the advective acceleration, which is related in part to the streamline curvature of the flow, may be computed using the reference frame ($\mathbf{s}$, $\mathbf{n}$). The advective acceleration is thus decomposed

$$\mathbf{u} \cdot \nabla\mathbf{u} = u\mathbf{s} \cdot \nabla(u\mathbf{s}) = u\delta(u\mathbf{s})/\delta s = \delta(u^2/2)/\delta s\mathbf{s} + u^2\kappa\mathbf{n} \quad (13)$$

into advective tangential and centripetal (normal) accelerations. Here $\delta/\delta s \equiv \mathbf{s} \cdot \nabla$ is the directional derivative along **s** and κ is the streamline curvature defined as $\kappa = \mathbf{k} \cdot \nabla \times \mathbf{s}$ (or by the Frenet-Serret formula $\delta\mathbf{s}/\delta s = \kappa\mathbf{n}$). Since the advective acceleration at 13 m (Fig. 12) has a large **n** component (normal to **u**), we see that it is related more to changes in direction than to changes in speed along the streamlines. (Though we only show the distributions at 13 m, these results apply to the whole water column down to 200 m.) The **n** component of the advective acceleration reduces the **n** component of the term, $\mathbf{u} \cdot \nabla\mathbf{u} + f\mathbf{k} \times \mathbf{u}$, in such a way that it is closer to the **n** component of the pressure anomaly force $-\mathbf{n} \cdot \nabla\Psi$. This centripetal-like acceleration to the right of the current direction is expected in gradient-balanced, supergeostrophic flows. We observe, however, very clearly in surveys 1 and 2, that $\mathbf{u} \cdot \nabla\mathbf{u}$ and $f\mathbf{k} \times \mathbf{u}$ are not exactly antiparallel, so a contribution also exists in the **s** direction.

3) THE QG VERTICAL VELOCITY AND THE VERTICAL ADVECTION OF **U**

In order to obtain the QG vertical velocity we employ the QG omega equation [ω equation; see Viúdez et al. (1996c) for a recent discussion on the generalized form of this equation and its QG approximation]. The QG ω equation in the f plane can be written as

$$\nabla \cdot (2\mathbf{Q}^g + b_{,z}\nabla w^{QG}) = f^2 w^{QG}{}_{,zz}, \quad (14)$$

where $\mathbf{Q}^g \equiv \nabla\mathbf{u}^g \cdot \nabla b$, $b \equiv g\rho^{-1}{}_0\rho$, and w^{QG} is the QG vertical velocity. When $\mathbf{Q}^g$ is known, (14) results in an equation for w^{QG}. To solve (14) it is usually assumed that $\mathbf{u}^g = \mathbf{0}$ at the bottom layer of the three-dimensional domain. This assumption results in $\mathbf{Q}^g = \mathbf{0}$, so $\nabla \cdot \mathbf{Q}^g = 0$ on that bottom layer, which constrains the possible spatial changes of w^{QG} at the lower levels. On the other hand, note that simple substitution of measured **u** in place of $\mathbf{u}^g$ in $\mathbf{Q}^g$ and solving (14) may be inconsistent with neglecting other non-QG terms from which (14) is derived. Since due to (7) $\mathbf{Q}^g$ can also be written as $\nabla\mathbf{u}^g \cdot (f\mathbf{k} \times \mathbf{u}^g{}_{,z})$, another inconsistency may arise when **Q** vectors are computed from **u** as $\nabla\mathbf{u} \cdot (f\mathbf{k} \times \mathbf{u}_{,z})$. This substitution has no theoretical basis since the generalized form of $\mathbf{Q}^g$ (i.e., consistent with the primitive equations) is $\mathbf{Q} \equiv \nabla\mathbf{u} \cdot \nabla b$.

The QG ω equation (14) was solved using $\mathbf{u}^g = \mathbf{0}$ at the bottom layer as discussed above, along with the common zero boundary conditions on w^{QG} at the bottom, top, and lateral boundaries in a similar way to that described in Viúdez et al. (1996a). See also Allen and Smeed (1996) for a discussion on the significance of the choice of boundary conditions. The resulting w^{QG} field at 100 m (Fig. 13) presents maximum value of 40–50 ($\times 10^{-5}$ m s^{-1}). The vertical velocity obtained by data assimilation in a numerical model using digital filter initialization, as in Viúdez et al. (1996b) (not shown), produces a similar field of vertical motion, thus indicating that the QG assumption is not critical for this problem. The vertical advection of horizontal velocity ($w^{QG}\mathbf{u}_{,z}$) is shown in Fig. 14. Typical maximum values reach 3×10^{-6} m s^{-2}, which is one order of magnitude smaller than the horizontal advective acceleration.[1]

The vertical shear distribution (Fig. 15) shows that $\mathbf{u}_{,z}$ is almost everywhere parallel to the current **u** itself (cf. Fig. 8a). Since $\mathbf{u}_{,z}$ is mostly directed along the flow, alongflow $w^{QG}\,\mathbf{u}_{,z}$ vectors mean positive w^{QG} (upward motion). Counterflow $w^{QG}\mathbf{u}_{,z}$ vectors mean negative w^{QG} (downward motion). This vertical advection has however little importance in the momentum balance and the results concerning the computation of $\mathbf{I}_0$ and $\mathbf{I}_1$ should not be affected, in general, if $w\mathbf{u}_{,z}$ were included and the w and w^{QG} patterns were different (the order of magnitude being similar). Note, however, that in some specific areas the vertical advection may be a significant part of the advective acceleration (e.g., in the NE region in cruise survey 3: cf. Fig. 14c with Fig. 12c). Since this occurs when the advective acceleration is small, the contribution of the vertical advection to the momentum balance will continue having little significance. It is also important to note that the use of "absolute" geostrophic velocities defined by (4) does not change the pattern of $\nabla \cdot \mathbf{Q}^g$ because the divergence of $\nabla\mathbf{u}^g \cdot \nabla b$ at $z = z_1 = -253$ m with $\mathbf{u}^g(\mathbf{x}, z_1) \equiv \alpha_0 f^{-1}\mathbf{k} \times \nabla P(\mathbf{x}, z_1)$ is an order of magnitude smaller than $\nabla \cdot \mathbf{Q}^g$ at $z = -100$ m. Therefore use of "absolute" geostrophic velocities in the ω equation does not have an important effect on the resulting w^{QG} in the Alboran Sea because, as we have seen, 253 m is an approximate "level of no motion."

4) THE DYNAMICAL IMBALANCES

The geostrophic ($\mathbf{I}_0$) and the gradient ($\mathbf{I}_1$) imbalances at 100 m are plotted, for the three cruises, in Fig. 16. The geostrophic imbalance reaches typical maximum values of 5×10^{-5} m s^{-2} at 13 m (2.5×10^{-5} m s^{-2} at 100 m, not shown). The $\mathbf{I}_0$ vectors are in many places directed toward the center of the WAG. Consequently, the gradient imbalance $\mathbf{I}_1$, which considers the advective acceleration, is significantly smaller, being in magnitude about half that of $\mathbf{I}_0$. In surveys 1 and 2 the gradient imbalance in the WAG is smaller than 1×10^{-5} m s^{-2}.

The gradient imbalance at the reference level $\mathbf{I}_1(\mathbf{x}, z_1)$ in survey 1, equal to $-(\mathbf{u} \cdot \nabla\mathbf{u} + f\mathbf{k} \times \mathbf{u})|_{z=z_0}$ (Fig. 17), has typical magnitudes of 0.6×10^{-5} m s^{-2}, that is, about 10 times smaller than the pressure anomaly gradient term at 13 m (Fig. 10). This distribution $\mathbf{I}_1(\mathbf{x}, z_1)$ consists primarily of the (minus) Coriolis acceleration since at this depth the advective acceleration is one order of magnitude smaller [$O(0.02 \times 10^{-5}$ m s$^{-2})$]. Assuming that $\mathbf{u}_{,t}(\mathbf{x}, z_0)$ is negligible in comparison with the pressure gradient term and the Coriolis acceleration, $\mathbf{I}_1(\mathbf{x}, z_1)$ is, in the absence of friction [see (8)], equal to the pressure gradient term at the reference level $\alpha_0 \nabla P(\mathbf{x}, z_0)$. The values of $\alpha_0 \nabla P(\mathbf{x}, z_0)$ so computed are therefore consistent with the advective timescale (local and advective acceleration are of the same order and negligible). Since $\mathbf{I}_0$ and $\mathbf{I}_1$ at 100 m (not shown) are about 4 and 2 times larger, respectively, than the pressure gradient term at the reference level, $\alpha_0 \nabla P(\mathbf{x}, z_0)$ (Fig. 17), the computation of the imbalances is not too sensitive to the choice of the reference level if this is taken below 200 m.

In general the gradient imbalance is larger in the AJ than in the WAG. A vertical section of $|\mathbf{I}_1|$ (Fig. 18) shows that the larger $|\mathbf{I}_1|$ values occur in the upper AJ, while in the WAG the gradient imbalance is smaller than 1×10^{-5} m s^{-2}. Note also that $\mathbf{I}_0$ and $\mathbf{I}_1$ for cruise survey 3 are larger than for surveys 1 and 2. The vertical dependence of $\langle|\mathbf{I}_1|/|\mathbf{I}_0|\rangle$ (Fig. 19) shows that the gradient imbalance is, in average, as small as 60% of the geostrophic imbalance at 50 m for surveys 1 and 2, where $\langle|\mathbf{I}_1|\rangle < \langle|\mathbf{I}_0|\rangle$ in the entire water column. The different dynamical situation for the last cruise (survey 3) could be related to the presence of a large local acceleration $\mathbf{u}_{,t}$ associated with a rapidly changing circulation pattern, which is also supported by the large values of $\nabla \cdot \mathbf{u}$ computed from survey 3 (appendix A).

It is noteworthy that the gradient imbalance is in many places tangent to the flow (i.e., it tends to be zonal) meaning that the AJ experiences alongflow fluctuations. These alongflow accelerations could be related to the waves that originate in the Strait of Gibraltar (Perkins et al. 1990).

5) THE TEMPORAL VARIABILITY

Since each field survey typically lasted several days and the imbalances computed above are of the same order of magnitude as the advective acceleration (cf. Figs. 16 and 12), there is a potential problem in assuming that the surveys are synoptic (i.e., in assuming $\mathbf{u}_{,t} \sim \mathbf{O}$). In order to address this potential problem in an experimental way we need reliable estimates of $\mathbf{u}_{,t}$. Although there are three consecutive surveys of the velocity field available, it is not appropriate to obtain two $\mathbf{u}_{,t}$ fields as $\Delta\mathbf{u}/\Delta t$ computed from simple time differentiation $(\mathbf{u}_{\text{survey2}} - \mathbf{u}_{\text{survey1}})/\Delta t_1$ and $(\mathbf{u}_{\text{survey3}} - \mathbf{u}_{\text{survey2}})/\Delta t_2$ because the (average) time interval between cruises (4 and 3 days) is too large to capture this higher-frequency variability important in the momentum balance (see appendix B). To estimate $\mathbf{u}_{,t}$ we therefore use current meter data deployed in the AJ and WAG in 1982 (Kinder 1984; Parrilla et al. 1986; Perkins et al. 1990). Here we will focus on two aspects of the $\mathbf{u}$ time series (Fig. 20). The first one is the presence of short period waves (semidiurnal and diurnal) in the AJ. The local acceleration $\mathbf{u}_{,t}$ due to these short period disturbances has an order of magnitude of 10^{-5} m s^{-2} and is therefore comparable to the $\mathbf{I}_1$ values at this depth (67 m, see Fig. 18). The temporal scale of $\mathbf{u}_{,t}$ is only several hours however, meaning that this local acceleration is responsible both for a part of the gradient imbalance in the AJ, and for the fact that this I_1 pattern must be considered not synoptic but rather only quasi synoptic or piecewise synoptic (because every leg was completed in about six hours).

The second point concerns the large space scale of the AJ–WAG system. During the two weeks when the WAG was not present in the western Alboran basin (Fig. 20), the AJ took a southward path immediately after crossing the Strait of Gibraltar, and therefore its signal was absent in the current meter moorings. The timescale of this phenomenon is a few days (the decrease of $\mathbf{u}$ vectors in the second week in Fig. 20), and therefore the local acceleration is $\Delta u/\Delta t \sim 10^{-6}$ m s^{-2},

which is small compared to the advective acceleration of the AJ–WAG system and, therefore to the $\mathbf{I}_1$ values. Similarly, wind forcing (or Ekman flow), which may contribute to the imbalance near the surface, would also supply a body force (per unit mass) to the upper 100 m of water that would be no larger than 10^{-6} m s^{-2}. Thus, the gradient imbalance is mostly related to the local acceleration of the short period features.

4. Discussion and conclusions

In this study we have carried out an analysis of the balance of horizontal momentum including the Coriolis and advective acceleration, the advection of horizontal velocity by the QG vertical velocity, and the pressure gradient. This analysis has been applied to observed density and horizontal velocity data taken in an open ocean current, namely, the Atlantic jet and anticyclonic gyre in the western Alboran Sea, which can be considered a good example of an oceanic current with a large vertical shear.

The results in the Alboran Sea show that the geostrophic imbalance reaches 5×10^{-5} m s^{-2} at the surface. The gradient imbalance is smaller, of order 2.5×10^{-5} m s^{-2}, and therefore gradient balance is considered the better estimate of the balance of horizontal momentum. The gradient imbalance is not uniform in the horizontal but rather is larger in the AJ than in the WAG. From this result it is inferred that the AJ current experiences larger variations (larger local acceleration) than the WAG current.

The gradient imbalance in the AJ seems to be related (by means of the momentum balance) to the local acceleration of short period features. This local acceleration has a temporal scale of about 8 h; thus the gradient imbalance field obtained is considered not to be synoptic, but only piecewise synoptic. The important issue is, however, not to determine if the data are synoptic or not in an absolute way, but rather to determine how the pattern and order of magnitude of every derived quantity (especially in our case the gradient imbalance) are affected by the sequential sampling of an unsteady flow.

When dealing with the role played by the local acceleration in any study of the momentum balance using conventional cruise data, it is convenient to distinguish between (i) the magnitude of $\mathbf{u}_{,t}$ relative to the other terms in the balance of momentum (with every term in this balance computed from synoptic data) and (ii) the influence of $\mathbf{u}_{,t}$ (temporal variability of the current) on the synopticity of the measured $\mathbf{u}$ field, thus on the advective acceleration, and consequently on the momentum balance. Here we have found that for cruise surveys 1 and 2 the computed advective acceleration is responsible for 40% of the geostrophic imbalance at 50 m [from $\mathbf{I}_0 + \mathbf{u} \cdot \nabla\mathbf{u} = \mathbf{I}_1$ and $\langle\mathbf{I}_0\rangle \approx 0.6\langle\mathbf{I}_1\rangle$ at 50 m (Fig. 19) it is deduced that $\langle\mathbf{u} \cdot \nabla\mathbf{u}\rangle \approx 0.4\langle\mathbf{I}_0\rangle$]. Thus, despite the high-frequency waves, problem (ii) did not invalidate the use of $\mathbf{u} \cdot \nabla\mathbf{u}$ for the study of the momentum balance, probably because part of the influence of the high-frequency motion in the sequentially sampled data is removed from the shorter scales during the spatial interpolation process (i.e., during the data analysis). These conclusions concerning the larger influence of the temporal variability in cruise survey 3 are also supported by the larger values of divergence computed from the velocity data in this last cruise (see appendix A).

The vertical advection of horizontal velocity is found to be negligible in the momentum balance. The vertical velocity obtained (order of 20×10^{-5} m s^{-1}) is smaller in magnitude than that found in Gulf Stream meanders by Lindstrom and Watts (1994). They found, using the vorticity equation, maximum vertical velocities of 10–20 ($\times 10^{-4}$ m s^{-1}) associated with strong meanders [these results were verified by direct observations using isopycnal (RAFOS) floats]. Allen and Smeed (1996), also using the QG ω equation, found maximum vertical velocities of 10×10^{-4} m s^{-1} associated with meanders and eddies of the Iceland–Færœ Front. The vertical scale of the AJ–WAG system (250 m) is, of course, smaller than that of the Gulf Stream and the Iceland–Færœ Front, so we would expect vertical velocities to be smaller as well.

Future experimental work devoted to refinements of the approach based on the direct analysis of the momentum budget could include also simultaneous current meter observations as well as additional forcing terms other than the pressure gradient (e.g., wind stress, tidal forcing, coastal boundary conditions, etc.). Future data analysis in this direction will also be able to obtain information about the relative importance of the pressure gradient term at the reference level and the contribution of the frictional processes.

Acknowledgments

We are especially grateful to D. Gomis and A. Mehra for valuable discussions on the analysis and interpretation of the data, to J. Tintoré for the use of the OMEGA data, and to H. Perkins, B. Teague, and the Naval Oceanographic Office (US) for having made available to us the current meter data of the “Donde va?” experiment. We also thank all the people onboard the R/V *Hespérides* as well as the Moroccan authorities for their courtesy and assistance. Encouragement and very constructive comments from two anonymous reviewers are also greatly appreciated. Support for this study was obtained

through a contract (AV) from the Ministerio Español de Educación y Cultura, from the Office of Naval Research Code 322 OM (RLH), and through E.C. project OMEGA (MAS3-CT-95-0001). This support is gratefully acknowledged.

REFERENCES

Allen, J. T., and D. A. Smeed, 1996: Potential vorticity and vertical velocity at the Iceland–Færœs Front. *J. Phys. Oceanogr.*, **26,** 2611–2634.. Find this article online

— ,and Coauthors, 1997: Upper ocean underway operations on BIO *Hespérides* cruise OMEGA–ALGERS (cruise 36) using SeaSoar and ADCP 30/9/96–14/10/96. Southampton Oceanography Centre Internal Document No. 17, 52 pp. [Available from Southampton Oceanography Centre, Waterfront Campus, Empress Dock, Southampton SO14 3ZH, United Kingdom.].

Brathset, A. M., 1986: Statistical interpolation by means of successive correction. *Tellus,* **38A,** 439–447..

Bucca, P. J., and T. H. Kinder, 1984: An example of meteorological effects on the Alboran Sea gyre. *J. Geophys. Res.,* **89,** 751–757..

Cano, N., 1978: Hidrología del Mar de Alborán en primavera-verano. *Bol. Inst. Esp. Oceanogr.*, **248,** 51–66..

Franke, R., 1988: Statistical interpolation by iteration. *Mon. Wea. Rev.*, **116,** 961–963.. Find this article online

Gascard, J. C., and C. Richez, 1985: Water masses and circulation in the western Alboran Sea and in the Straits of Gibraltar. *Progress in Oceanography*, Vol. 15, Pergamon, 157–216..

Gleizon, P., G. Chabert d'Hières, and D. Renouard, 1996: Experimental study of the Alboran Sea gyres. *Oceanol. Acta,* **19,** 499–511..

Heburn, G. W., and P. E. La Violette, 1990: Variations in the structure of the anticyclonic gyres found in the Alboran Sea. *J. Geophys. Res.,* **95,** 1599–1613..

JPOTS (Joint Panel on Oceanographic Tables and Standards), 1991: Processing of oceanographic station data. UNESCO, 138 pp..

Kinder, T. K., 1984: Net mass transport by internal waves near the Strait of Gibraltar. *Geophys. Res. Lett.*, **11,** 987–990..

La Violette, P. E., 1986: Short term measurements of surface currents associated with the Alboran Sea during Dónde Va? *J. Phys. Oceanogr.*, **16,** 262–279.. Find this article online

Lanoix, F., 1974: Projet Alboran, etude hydrologique et dynamique de la Mer d'Alboran. Tech. Rep. 66, NATO, 39 pp. plus 32 figs. [Available from NATO Subcommittee in Oceanographic Research, DK-2100 Copenhagen, Denmark.].

Lindstrom, S. S., and D. R. Watts, 1994: Vertical motion in the Gulf Stream near 68°W. *J. Phys. Oceanogr.*, **24,** 2321–2333.. Find this article online

Lynch, P., 1989: Partioning the wind in a limited domain. *Mon. Wea. Rev.*, **117,** 1492–1500.. Find this article online

Parrilla, G., and T. H. Kinder, 1987: The physical oceanography of the Alboran Sea. Reports in Meteorology and Oceanography 40, Vol. 1, 143–184. [Available from Oceanographic Group, Division of Applied Sciences, Harvard University, Cambridge, MA 02138.].

— ,— ,and R. H. Preller, 1986: Deep and Intermediate Mediterranean Water in the western Alboran Sea. *Deep-Sea Res.*, **33,** 55–88..

Perkins, H., T. Kinder, and P. E. La Violette, 1990: The Atlantic inflow in the western Alboran Sea. *J. Phys. Oceanogr.*, **20,** 242–263.. Find this article online

Pollard, R. T., and J. F. Read, 1989: A method for calibrating shipmounted Acoustic Doppler Profilers, and the limitations of gyro compasses. *J. Atmos. Oceanic Technol.*, **6,** 859–865..

Speich, S., G. Madec, and M. Crépon, 1996: A strait outflow circulation process study: The case of the Alboran Sea. *J. Phys. Oceanogr.*, **26,** 320–340.. Find this article online

Vázquez-Cuervo, J., J. Font, and J. J. Martínez-Benjamín, 1995: Observations on the circulation in the Alboran Sea using *ERS1* altimetry and sea surface temperature data. *J. Phys. Oceanogr.*, **26,** 1426–1447.. Find this article online

Viúdez, A., and R. L. Haney, 1997: On the relative vorticity of the Atlantic jet in the Alboran Sea. *J. Phys. Oceanogr.*, **27,** 175–185.. Find this article online

— ,J. Tintoré, and R. L. Haney, 1996a: Circulation in the Alboran Sea as determined by quasi-synoptic hydrographic observations. Part

I: Three-dimensional structure of the two anticyclonic gyres. *J. Phys. Oceanogr.*, **26,** 684–705.. Find this article online

— ,R. L. Haney, and J. Tintoré, 1996b: Circulation in the Alboran Sea as determined by quasi-synoptic hydrographic observations. Part II: Mesoscale ageostrophic motion diagnosed through density dynamical assimilation. *J. Phys. Oceanogr.*, **26,** 706–724.. Find this article online

— ,J. Tintoré, and R. L. Haney, 1996c: About the nature of the generalized Omega equation. *J. Atmos. Sci.*, **53,** 787–795.. Find this article online

— ,J.-M. Pinot, and R. L. Haney, 1998: On the upper layer circulation in the Alboran Sea. *J. Geophys. Res.*, **103,** 21 653–21 666..

Whitehead, J. A., Jr., 1985: A laboratory study of gyres and uplift near the Strait of Gibraltar. *J. Geophys. Res.*, **90,** 7045–7060..

— ,and A. R. Miller, 1979: Laboratory simulations of the gyre in the Alboran Sea. *J. Geophys. Res.*, **84,** 3733–3742..

APPENDIX A

5. Errors in the Analyzed Velocity Field

For typical vertical changes in the vertical velocity in the Alboran Sea of $O(10^{-4}$ m s$^{-1})$ on a vertical length scale $\Delta z \sim$ 100 m, and horizontal length scale for the horizontal velocity $\Delta x \sim 20 \times 10^3$ m, the incompressibility condition implies that horizontal changes in the divergent part of the horizontal velocity field scales as $\Delta u = \Delta w\, \Delta x/\Delta z \sim 2$ cm s^{-1}, which is similar to the ADCP accuracy. On the other hand the distribution of $\nabla \cdot \mathbf{u}$ on vertical section F for cruise survey 1 (Fig. A1) shows that $|\nabla \cdot \mathbf{u}| = O(10^{-6}$ s$^{-1})$, which for $\Delta z \sim 100$ m implies vertical changes in the vertical velocity Δw of $O(10^{-4}$ m s$^{-1})$, which is the same order of magnitude (though w values computed from $w_{,z} = -\nabla \cdot \mathbf{u}$ are two or three times larger than w^{QG}, as the mesoscale vertical velocity obtained here in the Alboran Sea using QG theory as well as in Viúdez et al. (1996a). Note that the relatively small values of $\nabla \cdot \mathbf{u}$ are in part due to the interpolation procedure, which does not allow small-scale structures to be present in the velocity data. On the other hand, note that the correct divergence field should reverse sign along the vertical, which is not the case of the directly computed divergence field, and as a result, the directly computed $\nabla \cdot \mathbf{u}$ and the differential quasigeostrophic vertical velocity obtained from the QG omega equation are not similar. Thus, we conclude that no significant part of the true divergence of the velocity field remains in the interpolated velocity data. For the above two reasons (divergent part of the velocity field being similar to the ADCP accuracy, but divergence of the interpolated ADCP data being of the expected order of magnitude), it has been assumed in this work, as it is usually done concerning ADCP data, that the experimental error in $\mathbf{u}$ makes calculation of $\nabla \cdot \mathbf{u}$ unrealistic. Note that errors in the computed $\nabla \cdot \mathbf{u}$ field include sampling errors due to the existence of higher-frequency motion and the nonsynopticity of the data (probably the largest contributor) as well as instrumental errors, and furthermore are affected also by the interpolation procedure.

In order to account for this fact it is necessary to know how derived quantities are affected by the unrealistic $\nabla \cdot \mathbf{u}$ values. For example, to compute how much the advective acceleration is affected by $\nabla \cdot \mathbf{u}$ we can use the kinematic identity $\mathbf{u} \cdot \nabla\mathbf{u} = \nabla \cdot (\mathbf{uu}) - \mathbf{u}\nabla \cdot \mathbf{u}$ for the dyadic $\mathbf{uu}$. It is therefore assumed that the field $\mathbf{u}\nabla \cdot \mathbf{u}$ is an estimate of the error in $\mathbf{u} \cdot \nabla\mathbf{u}$ due to the unrealistic $\nabla \cdot \mathbf{u}$ values. The effect in the $\mathbf{I}_1$ field due to the term $\mathbf{u}\nabla \cdot \mathbf{u}$ is the error field $\delta I_1 \equiv |\mathbf{u}\nabla \cdot \mathbf{u}|$.

The horizontal average of the absolute value of the horizontal divergence, $\langle|\nabla \cdot \mathbf{u}|\rangle$, is shown in Fig. A2. It reaches maximum values of 15–22 ($\times 10^{-6}$ s^{-1}) at the surface, and minimum values of 5–8 ($\times 10^{-6}$ s^{-1}) below 200 m. This means that, with $u = O(0.5$ m s$^{-1})$ at 100 m, $\delta I_1 = O(5 \times 10^{-6}$ m s$^{-2})$, which is about four times smaller than the maximum significant values of $\mathbf{I}_1$ (Fig. 18). The important point is however that the averaged divergence field was minimal at all depths for survey 1. Thus, if $\nabla \cdot \mathbf{u}$ is considered an error field, survey 1 provided the optimal dataset for the analysis of the theory presented in this study. These large values of $\langle|\nabla \cdot \mathbf{u}|\rangle$ were probably caused by the errors induced by the rapidly changing current field in the upper Alboran Sea during surveys 2 and 3 (addressed in section 3).

The difficulty associated with the divergence of the horizontal velocity could be avoided by decomposing the velocity field, following Helmholtz's theorem, into rotational ($\mathbf{u}_\phi \equiv \mathbf{k} \times \nabla\phi$) and divergent ($\mathbf{u}_\chi \equiv \nabla\chi$) components and considering only the rotational (nondivergent) $\mathbf{u}_\phi$ in the analysis. However, in a limited domain this decomposition is not unique but

depends on the boundary conditions chosen for the functions Φ and χ of the vector fields, and therefore new assumptions would have to be introduced (see Lynch 1989). The above decomposition can however be used to estimate the order of magnitude of the error in the interpolated velocity field consistent with the fact that $\nabla \cdot \mathbf{u}$ is considered an error field. Solving the equation $\nabla^2\chi = \nabla \cdot \mathbf{u}$, with the boundary condition $\chi = 0$, the error field in the velocity is obtained as $\mathbf{u}_\chi \equiv \nabla\chi$. Since the boundary condition that we use, $\chi = 0$, minimizes the spatially averaged kinetic energy of $\mathbf{u}_\chi$ in the domain (Lynch 1989), the $|\mathbf{u}_\chi|$ field obtained may be considered as a lower bound of the error. The resulting magnitude of $\mathbf{u}_\chi$ (not shown) is 5–8 cm s^{-1}. This error in the interpolated velocity field includes instrumental errors, errors due to the interpolation procedure, and errors due to the nonsynopticity of the data [since $\mathbf{u}(\mathbf{x})$ is considered synoptic when $\nabla \cdot \mathbf{u}$ is computed]. Its order of magnitude is the same as that obtained by cross-validation of the ADCP data (D. Gomis 1997, personal communication). Note that an error of $\delta u \sim$ 8 cm s^{-1} produces an error in the Coriolis acceleration of $f\delta u \sim 0.6 \times 10^{-5}$ m s^{-2}, which is still smaller than the maximum values of the imbalance terms $\mathbf{I}_0$ and $\mathbf{I}_1$ at 100 m.

APPENDIX B

6. The Large-Scale Local Acceleration

Two estimates of the local acceleration ($\Delta\mathbf{u}/\Delta t$) computed from simple time differentiation $(\mathbf{u}_{survey2} - \mathbf{u}_{survey1})/\Delta t_1$ and $(\mathbf{u}_{survey3} - \mathbf{u}_{survey2})/\Delta t_2$, assuming an average interval time of $\Delta t_1 = 4.2$ and $\Delta t_2 = 3.0$ days, are shown in Fig. B1. The large $\Delta\mathbf{u}/\Delta t$ vectors in the northern part of Fig. B1a [pointing in the westward (eastward) direction] represent the temporal decrease (increase) of the velocity field in this area between samplings of surveys 1 and 2 related to the already mentioned southward (northward) shift of the AJ in the western (eastern) part of the domain. The second $\Delta\mathbf{u}/\Delta t$ field (Fig. B1b) shows again this southward shift of the AJ current in the western part and the local clockwise rotation of $\mathbf{u}$ in the northeastern corner (visible as northward pointing $\Delta\mathbf{u}/\Delta t$ vectors). The important point here, however, is that the local acceleration so computed [maximum values between 0.1 and 0.3 ($\times 10^{-5}$ m s^{-2}) at 13 m] is an order of magnitude smaller than the advective acceleration (Fig. 12). If this order of magnitude of $\mathbf{u}_{,t}$ were correct (which assumes a linear evolution between the different velocities, thereby neglecting high-frequency tidal motions), we would not be able to close the momentum budget (8) up to a reasonably small residual without resorting to some other forcing term such as wind stress. But such a term, acting over 100 m of water, is also no larger than 10^{-6} m s^{-2}.

Figures

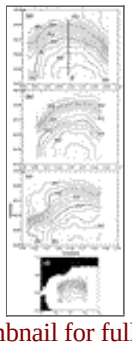

Click on thumbnail for full-sized image.

Fig. 1. Potential density (σ_θ) distribution at $z = -100$ m for the three consecutive surveys [(a) survey 1, (b) survey 2, and (c) survey 3 respectively on 1–4, 6–8, and 9–11 Oct 1996]. Dots indicate theSeaSoar interpolated stations. The large dot indicates the location of current meter 151. Vertical section F is referenced. Labels longitude and latitude in degrees. Contour interval $\Delta = 0.2$ σ_θ. The little black area in the northwestern corner represents a small piece of land. (d) Shows the location of (a) relative to the Strait of Gibraltar, Iberian (north), and African (south) coasts.

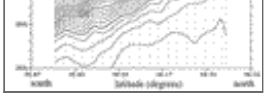

Click on thumbnail for full-sized image.

Fig. 2. Potential density (σ_θ) distribution at vertical section F for survey 1 (referenced in Fig. 1). The dots indicate the interpolated SeaSoar data. Contour interval $\Delta = 0.1\ \sigma_\theta$.

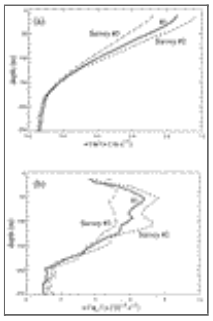

Click on thumbnail for full-sized image.

Fig. 3. Vertical dependence of the horizontally averaged magnitude of the (a) horizontal velocity $\langle|\mathbf{u}|\rangle$ and (b) vertical shear $\langle|\mathbf{u}_{,z}|\rangle$ for the three surveys.

Click on thumbnail for full-sized image.

Fig. 4. Distribution of the magnitude of the vertical shear $|\mathbf{u}_{,z}|$ at vertical section F (referenced in Fig. 1) for (a) survey 1, (b) survey 2, and (c) survey 3. Contour interval $\Delta = 2 \times 10^{-3}\ \mathrm{s}^{-1}$ (contour of $1 \times 10^{-3}\ \mathrm{s}^{-1}$ has also been included to better show where $|\mathbf{u}_{,z}|$ approaches zero). The dots indicate the interpolated SeaSoar stations.

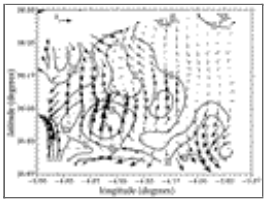

Click on thumbnail for full-sized image.

Fig. 5. Horizontal distribution at $z = -253$ m of the vertical shear $\mathbf{u}_{,z}$ for survey 1. Reference vector is $2 \times 10^{-3}\ \mathrm{s}^{-1}$. Only every other vector has been plotted. Isolines indicate the magnitude $|\mathbf{u}_{,z}|$ with $\Delta = 1 \times 10^{-3}\ \mathrm{s}^{-1}$.

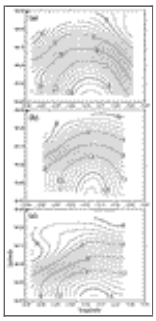

Click on thumbnail for full-sized image.

Fig. 6. Horizontal distribution of the geostrophic transport function $Q_{z_1}(\mathbf{x}, z)$, at depth $z = -13$ m and for the reference level $z_1 = -253$ m, for (a) survey 1, (b) survey 2, and (c) survey 3; $\Delta = 0.2 \times 10^6 \mathrm{m}^3\ \mathrm{s}^{-1}$.

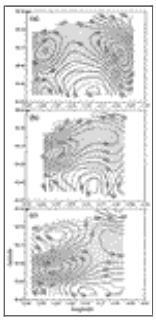

Click on thumbnail for full-sized image.

Fig. 7. Horizontal distribution of the geostrophic speed (dotted thick isolines with $\Delta = 10$ cm s^{-1}) and pressure anomaly [$\Psi(\mathbf{x}, z_1, z)$] isolines (continuous thin lines) at $z = -13$ m using a reference level $z_1 = -253$ m, for (a) survey 1, (b) survey 2, and (c) survey 3. The pressure anomaly field has been plotted just to indicate the direction of the geostrophic flow (tangent to the pressure anomaly isolines).

Click on thumbnail for full-sized image.

8. Horizontal distribution at $z = -13$ m of $\mathbf{u}$ (the interpolated ADCP velocity field) for (a) survey 1, (b) survey 2, and (c) survey 3. Reference vector is 100 cm s^{-1}. For clarity only every other vector has been plotted. Isolines indicate the speed $u \equiv |\mathbf{u}|$ with $\Delta =$ 10 cm s^{-1}.

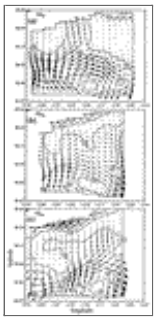

Click on thumbnail for full-sized image.

Fig. 9. Horizontal distribution at $z = -100$ m of the ageostrophic velocity field $\mathbf{u} - \mathbf{u}^g$ for (a) survey 1, (b) survey 2, and (c) survey 3. Reference vector is 20 cm s^{-1}. Only every other vector has been plotted. Isolines indicate the vector magnitude with Δ = 10 cm s^{-1}. The geostrophic velocity at the reference level has been neglected.

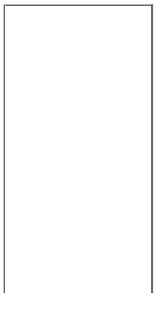

Click on thumbnail for full-sized image.

Fig. 10. Horizontal distribution at $z = -13$ m of the magnitude of the pressure anomaly gradient force $-\nabla\Psi(\mathbf{x}, z_1, z)$ for $z_1 = -253$ m (dotted thick isolines with $\Delta = 1 \times 10^{-5}$ m s^{-2}). The pressure anomaly field (Ψ, thin continuous isolines) has been plotted just to indicate the direction of the pressure anomaly force (normal to the pressure anomaly isolines with a northward component).

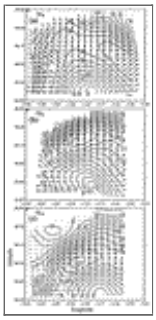

Click on thumbnail for full-sized image.

Fig. 11. Horizontal distribution at $z = -13$ m of the Coriolis acceleration field $f\mathbf{k} \times \mathbf{u}$ for (a) survey 1, (b) survey 2, and (c) survey 3. Reference vector is 10×10^{-5} m s^{-2}. Only every other vector has been plotted. Isolines indicate the magnitude $|f\mathbf{k} \times \mathbf{u}|$ with $\Delta = 1 \times 10^{-5}$ m s^{-2}.

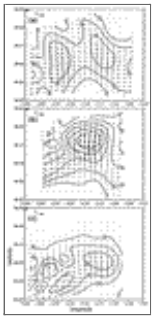

Click on thumbnail for full-sized image.

12. Horizontal distribution at $z = -13$ m of the advective acceleration field $\mathbf{u} \cdot \nabla\mathbf{u}$ for (a) survey 1, (b) survey 2, and (c) survey 3. Reference vector is 5×10^{-5} m s^{-2}. Only every other vector has been plotted. Isolines indicate the magnitude $|\mathbf{u} \cdot \nabla\mathbf{u}|$ with $\Delta = 1 \times 10^{-5}$ m s^{-2}.

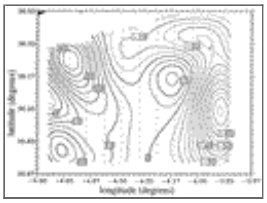

Click on thumbnail for full-sized image.

Fig. 13. Horizontal distribution at $z = -100$ m of the QG vertical velocity w^{QG} for survey 1; $\Delta = 5 \times 10^{-5}$ m s^{-1}.

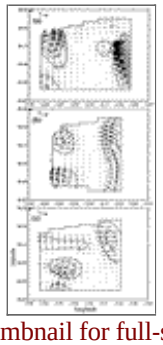

Click on thumbnail for full-sized image.

Fig. 14. Horizontal distribution at $z = -100$ m of the vertical advection of horizontal velocity by the QG vertical velocity ($w^{QG}\mathbf{u}_{,z}$)

for (a) survey 1, (b) survey 2, and (c) survey 3. Reference vector is 2×10^{-6} m s^{-2}. Only every other vector has been plotted. Isolines indicate the magnitude $|w^{QG}\mathbf{u}_{,z}|$ with $\Delta = 1 \times 10^{-6}$ m s^{-2}.

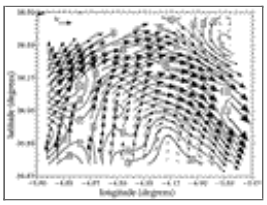

Click on thumbnail for full-sized image.

Fig. 15. Horizontal distribution at $z = -100$ m of the vertical shear $\mathbf{u}_{,z}$ for survey 1. Reference vector is 5×10^{-3} s^{-1}. Only every other vector has been plotted. Isolines indicate the magnitude $|\mathbf{u}_{,z}|$ with $\Delta = 1 \times 10^{-3}$ s^{-1}. Maximum $|\mathbf{u}_{,z1}$ values reach 10×10^{-3} s^{-1}.

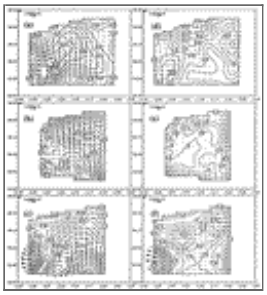

Click on thumbnail for full-sized image.

Fig. 16. Horizontal distribution at $z = -13$ m of the geostrophic imbalance $\mathbf{I}_0(\mathbf{x}, z_1, z)$ (a, b, and c), and the gradient imbalance $\mathbf{I}_1(\mathbf{x}, z_1, z)$, (d, e, and f)$_1$ with $z_1 = -253$ m, for the three surveys 1, 2, and 3, respectively. Reference vector is 5×10^{-5} m s^{-2}. Vectors close to the boundary stations have been removed because of the impossibility of obtaining realistic spatial derivatives there. Only every other vector has been plotted. Isolines indicate the vector magnitude with $\Delta = 0.5 \times 10^{-5}$ m s^{-2}.

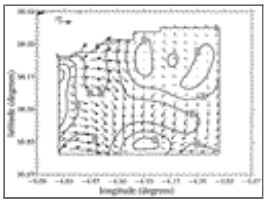

Click on thumbnail for full-sized image.

Fig. 17. Horizontal distribution of the gradient imbalance $\mathbf{I}_1(\mathbf{x}, z_1)$ at the reference level $z_1 = -253$ m in survey 1. Reference vector is 10×10^{-6} m s^{-2}. Only every other vector has been plotted. Isolines indicate the magnitude $|\mathbf{I}_1(\mathbf{x}, z_1)|$ with $\Delta = 1 \times 10^{-6}$ m s^{-2}.

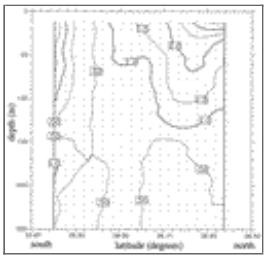

Click on thumbnail for full-sized image.

Fig. 18. Distribution at vertical section F for survey 1 (referenced in Fig. 1) of the magnitude of the gradient imbalance $|\mathbf{I}_1|$. $\Delta = 0.5 \times 10^{-5}$ m s^{-2}.

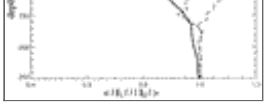

Click on thumbnail for full-sized image.

Fig. 19. Vertical dependence of the averaged ratio between the imbalances $\langle|\mathbf{I}_1|/|\mathbf{I}_0|\rangle$ for the three surveys.

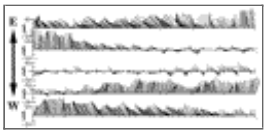

Click on thumbnail for full-sized image.

Fig. 20. Time series (five consecutive weeks with a sampling interval of 5 minutes) of the current meter 151 [positioned at 67-m depth on 36°01.5′N, 4°43.9′W (see Fig. 1a)]. During the third week the AJ current was not present in the current meter location [see Perkins et al. (1990) for detailed information]. Ticks interval is 1 day. The vertical axis is aligned with the east. Time interval between vectors is 30 minutes.

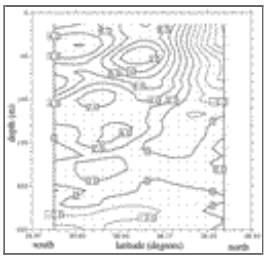

Click on thumbnail for full-sized image.

Fig. A1. Horizontal divergence ($\nabla \cdot \mathbf{u}$) distribution at vertical section F for survey 1 (referenced in Fig. 1). The dots indicate the interpolated ADCP data; $\Delta = 2 \times 10^{-6}$ s^{-1}.

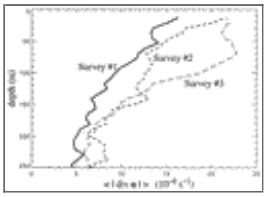

Click on thumbnail for full-sized image.

Fig. A2. The horizontal average of the absolute value of the horizontal divergence $\langle|\nabla \cdot \mathbf{u}|\rangle$ as a function of depth for the three surveys.

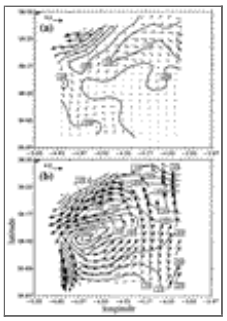

Click on thumbnail for full-sized image.

Fig. B1. Horizontal distribution at $z = -13$ m of the local acceleration field $\Delta\mathbf{u}/\Delta t$ computed by differencing the current data in surveys 1 and 2 (a) and surveys 2 and 3 (b). Reference vector is 0.2×10^{-5} m s^{-2}. Only every other vector has been plotted. Isolines indicate the magnitude $|\Delta\mathbf{u}/\Delta t|$ with $\Delta = 0.05 \times 10^{-5}$ m s^{-2}.

* Permanent affiliation: Department of Meteorology, Naval Postgraduate School, Monterey, California.

Corresponding author address: Prof. Robert L. Haney, Department of Meteorology, Naval Postgraduate School, Monterey, CA 93943-5114.

[1] The large QG vertical velocities diagnosed at the western and eastern boundaries (Fig. 13) are an artifact of the objective analysis scheme (D. Gomis and M. A. Pedder 1999, personal communication). The large values of $w^{QG}\mathbf{u}_{,z}$ at these boundaries (Fig. 14) are therefore artificial, which further supports neglecting vertical advection in the horizontal momentum budget.

E-mail: haneyrl@met.nps.navy.mil

top